Fig. 3.11 Maps of mineral potential derived from KD-modelling compared against known distribution of mineral occurrences. (a) SEDEX model shows that known deposits are localised within areas where less-permeable units are present. Favourability is dominated by lithological variation rather than fault control (note large 5km fault buffering). The model is not restrictive therefore wide areas may have potential for SEDEX-type mineralisation in the region. However, if we consider the relationship to clusters of small tonnage deposits and Century, the prospectivity may be constrained to areas where a similar spatial association occurs (e.g. the Kamarga Dome Area). This area records also elevated lithostratigraphic potential. (b) VS model with equal weighting for faults and lithological control (1km buffer chosen for faults). Most of the prospect/deposits occur in the northwestern part of the Lawn Hill Region. In contrast, the KD-model output for VS ore predicts the occurrence of mineralisation in the southeastern part of the Lawn Hill Region. This may be explained either as due to relative undiscovered sites in the favourable intervals or to local redistribution of syngenetic mineralisation that would justify the linkage of VS deposits to Century-style mineralisation in less favourable areas. (c, d, e) Enlargements showing chosen subsets with relative clusters of deposits/prospects.

3.5. Data driven modelling

The Weights of Evidence approach (WofE) (reviewed in Spiegelhalter, 1986; Bonham-Carter, 1994) was utilised to develop a Data-Driven model for the Lawn Hill Region. An advantage derived from the objectivity of this method is its exploratory nature. As it will be demonstrated in the following sections, the spatial association between known deposits and other geological patterns can be explored in detail using the WofE approach. This method, rather than relying on expert knowledge, defines the probability distribution of each evidential layer by estimating a positive and a negative weight for the degree of spatial association existing between the area distribution of deposits/prospects, and the pattern considered.

3.5.1. Datasets considered within the model and integration with GIS software

An initial phase involves data integration, usually carried out in a GIS environment. The datasets include either geo-referenced, vectorial or raster files with predefined resolution. For this case study, the DD-model considered geophysical datasets in addition to the layers considered in the KD-model. Data were provided by Zinifex Pty Ltd (Formerly Pasminco Pty Ltd) and Xstrata Pty Ltd. These include gravimetric, magnetic (TMI), and Radiometric Airborne Surveys (K-Th-U). Gravimetric and magnetic data provide information relative to deeper structures of the basement and the spatial distribution of igneous rocks, and also may locally aid identification of sulphide mineralisation. The radiometric spectra yield qualitative information on the spatial distribution of certain lithotypes; for instance, the siliciclastic rocks occurring in the study area contain abundant phyllosilicates and feldspars, so their distribution is matched by elevated K and Th signatures. U being a relatively immobile element in its hexavalent state is commonly concentrated in carbonaceous shales that are one of the most prospective lithotypes in the region.

A number of *a priori* assumptions are necessary to construct the model. A unit cell area of 0.1 km^2 was chosen for prospects and deposits, which represents an average size between the super large Century deposit (approx 2.25 km^2) and the smaller veins/lodes (e.g. Silver King, Watson's Lode) (approx. 0.05 to 0.1 km^2). The Prior probability (P_{prior}) expressed as the ratio between the area of known deposits/prospects and the total study area was estimated considering 87 Pb-Zn-Cu mineral occurrences although selecting an area of 0.1 km^2 generated a degree of overlap between some prospects. Overlapping

occurrences were interpreted as coeval and therefore overlapping pixels were counted as being part of a single prospect. This caused a reduction to 82 occurrences to account for the approx. 5.75 % of overlap within the model. Note that unit cell size does not reflect the real pixels of integrated raster layers. Pixel rescaling is implemented, because of the mathematical assumption in the Bayes calculations that have to respect the criterion of 1unit cell = 1 deposit (Carranza, 2002).

3.5.2. Phases of Weights of Evidence modelling

Three phases are fundamental to the Weights of Evidence approach:

(1) Contrast analysis that involves mathematical computation of Weights of Evidence for all the evidence considered, and includes cut-off determinations for buffer selection;
(2) combination of layers using the Bayes rule (e.g. Bonham-Carter, 1994); and
(3) conditional independence (CI) evaluation using multivariate statistical testing (e.g. χ^2, OT and New OT tests).

After the data assembly and establishment of preliminary assumptions, criteria standardization is required. This involves the weighting of evidence layers, and also a ranking of their degree of spatial association with known deposits. These two steps were accomplished using the WofE modeller (software developed by the author at James Cook University). This application has been compiled using Visual Basic Express 2005

integrating Bayesian algorithms. Handling of data and probability calculations are simplified by the use of a GUI (graphic user interface) in a Windows platform (Fig. 3.12).

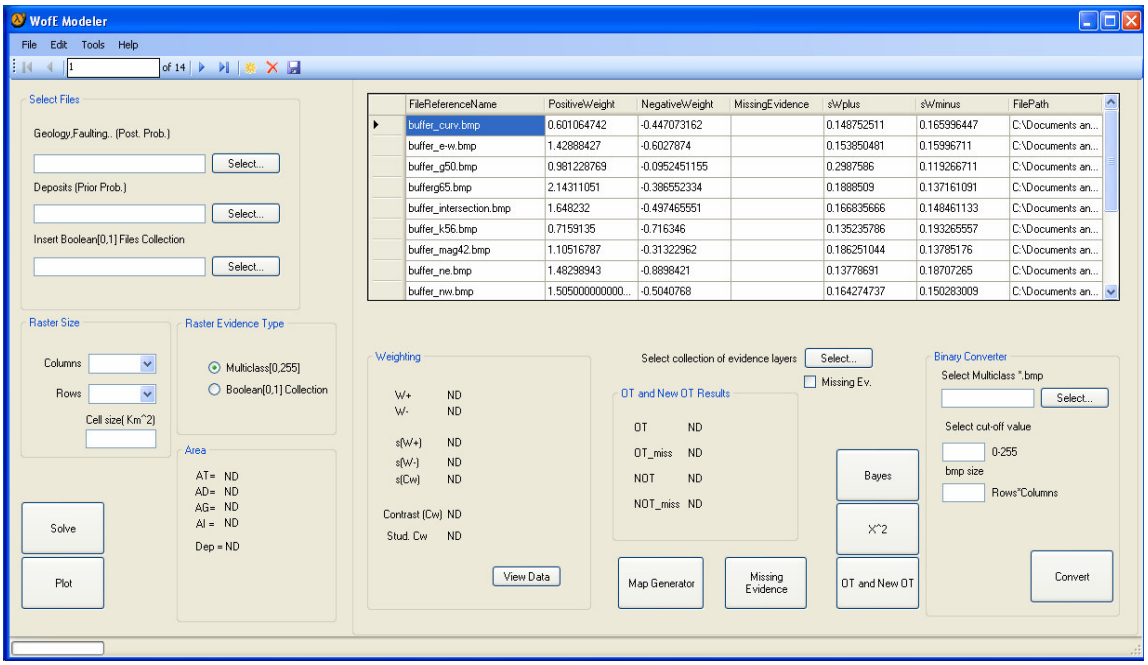

Fig. 3.12 Graphic User Interface (GUI) of the WofE modeller, which was used to perform Bayesian analysis and testing of CI assumptions (see text).

3.5.2.1.Standardization procedure

Algorithms and mathematical assumptions implemented in the WofE modeller are summarised in Appendix B. To measure spatial association the methodology suggested in Bonham-Carter (1994) was implemented, which is considered one of the most widely used for mineral potential mapping (Porwal et al., 2006).

3.5.2.2. Classification of spatial evidence

Three different approaches were utilised to evaluate the degree of correlation amongst geological features (e.g. faulting, lithotypes etc.) and mineralised areas. All of them are based on the Contrast (C) measure. The Contrast is expressed mathematically as the difference between positive and negative Weights of Evidence ($C = W_n^+ - W_n^-$, see Appendix B). It yields positive or negative values; suggesting correlation or inverse correlation. If the Contrast value is zero, there is no spatial association among geological features and deposits/prospects (see Bonham-Carter, 1994).

The methods adopted for the standardization of evidential layers were different, because of the different datasets utilised, and they can be distinguished as follows:

(1) Contrast analysis on multi-class layers obtained from simplification of pre-existing classes was applied to simplify the 32 lithostratigraphic subdivisions considered (see Fig. 3.3). Binary simplification was used before Bayesian analysis as it increases statistical robustness (Agterberg and Bonham-Carter, 2005). This procedure may involve discarding of classes displaying weaker correlation amongst patterns and known deposits (e.g. multiclass geophysical datasets, Paganelli et al., 2002);

(2) Contrast analysis based on cumulative buffers representing distance from geological features was considered for NW, NE, E-W faults, fault intersections, and points of maximum curvature (which represent a parameter similar to the measure of roughness; Blenkinsop et al., 2004). This approach progressively increases the area surrounding the geological pattern considered, providing multiple C values. Usually the maximum Contrast value is chosen. This variation

of Contrast is expressed as a function of distance in a graph (see Fig. 3.13). The Contrast (C) can be used to rank the importance of considered factors; for instance, to evaluate which fault orientations have greater mineral potential. One of the difficulties encountered in the definition of the best buffer was the presence of multiple maximum values for the Contrast (e.g. Fig. 3.13a and 3.13b). The presence of a multimodal distribution produces this type of output reflecting independent classes of spatial association. To improve the interpretation of Contrast curves it is convenient to plot the ratio between C and its standard deviation s(C), which is defined as studentised Contrast (Bonham-Carter, 1994). This parameter, being inversely proportional to error s(C), provides a better way to constrain spatial association and decide which maximum C has to be used for buffer standardization. Highest values of studentised Contrast reflect the best Contrast estimation although in some cases geological interpretation is required to select an appropriate buffer. Several buffer sizes are trialled to obtain the correct maximization of C. Here linear fuzzy membership functions were also used to increase the resolution of the Contrast's curves. This method provided better estimates for the C value and buffer size (conf. Fig. 3.14a with 3.14b). A correct representation of the Contrast is essential to avoid conditional dependences that violate the Bayes rule (see below); and

(3) Contrast analysis of multi-class data based on cumulative buffering, where the centre of each buffer is defined by plotting histograms representing the distribution of multiclass patterns intersecting deposit areas. When standardization is applied to geophysical datasets generally, a reclassification of

the original raster is required (Bonham-Carter et al., 1989; Paganelli et al., 2002). Property ranges are used for buffer definition. The reclassification procedure can be arbitrary, for example, visually the geologist can define certain classes of spatial association between property ranges and deposits. In contrast, a method was trialled in which the centre of the classes is determined by interpreting histogram plots of Boolean intersections of multiclass property layers with the deposit evidential layer. These provide a qualitative analysis of the distribution of peaks of correlation among certain pattern's classes and known mineral deposits (see Fig. 3.15). Both unimodal and multimodal distributions occur. Peak values of association were used for reclassification defining a new number of classes and their centre. The Contrast analysis based on cumulative buffers departing from these selected centres was implemented to define buffer size and Weights of Evidence. Multiclass data were then preserved reducing them to multiple binary files, representing both strong and weak trends of spatial correlation.

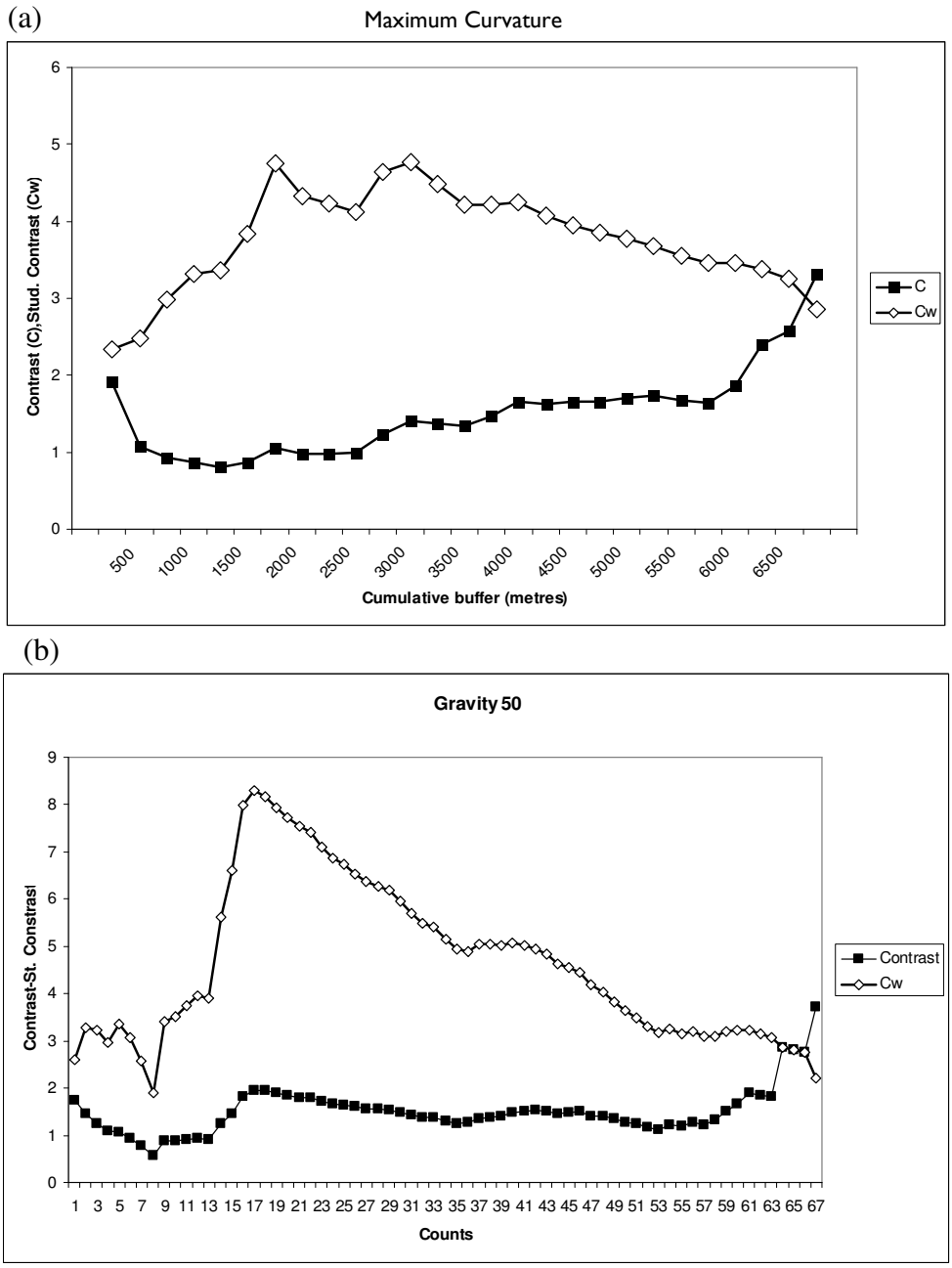

Fig. 3.13 Examples of output of contrast analysis and calculated studentised value (C_w) for the contrast measure (C). (a) Multiple maximum curvature values for C and C_w indicative of multiple spatial correlation of cluster of mineral deposits to certain buffers of the Maximum Curvature evidence layer. (b) Same type of correlation for the Gravity dataset suggesting a multimodal spatial association between certain gravimetric classes and the mineral deposit layer.

(a) NE faults 250 m buffer interval

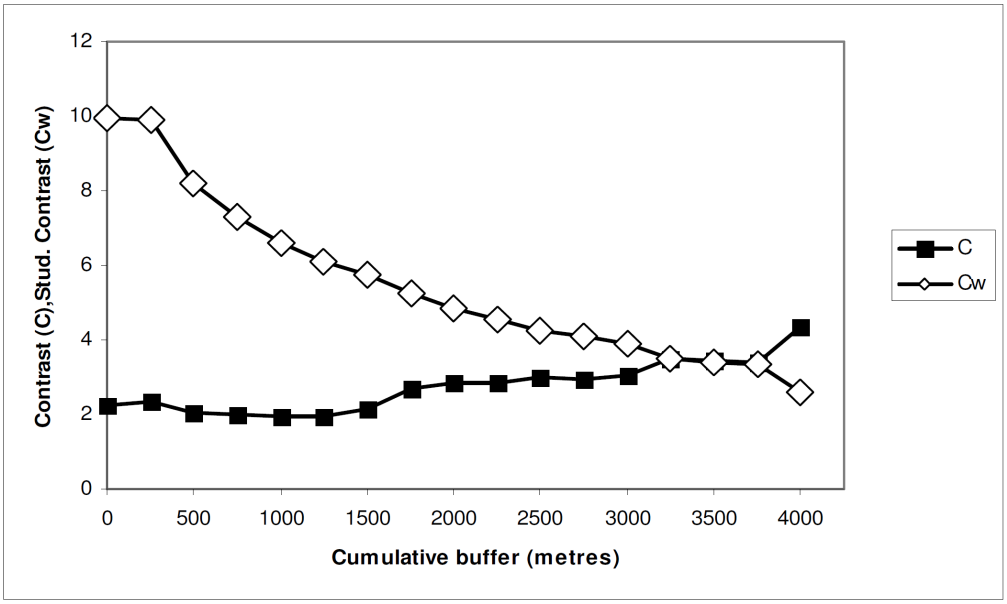

(b) NE faults fuzzy linear rescaling with 16.7 m buffer

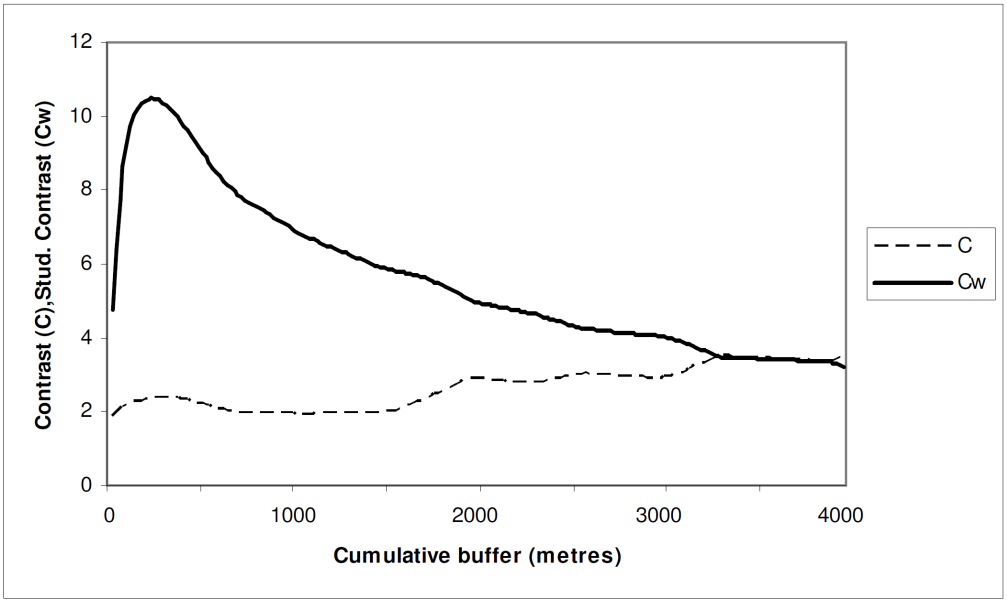

Fig. 3.14 Comparison of conventional contrast approach using constant buffers of 250 m interval with Contrast analysis performed using dynamic rescaling based on fuzzy linear functions. The smooth result allows better selection of the buffer, which reduces the possibility of overestimation of posterior probabilities.

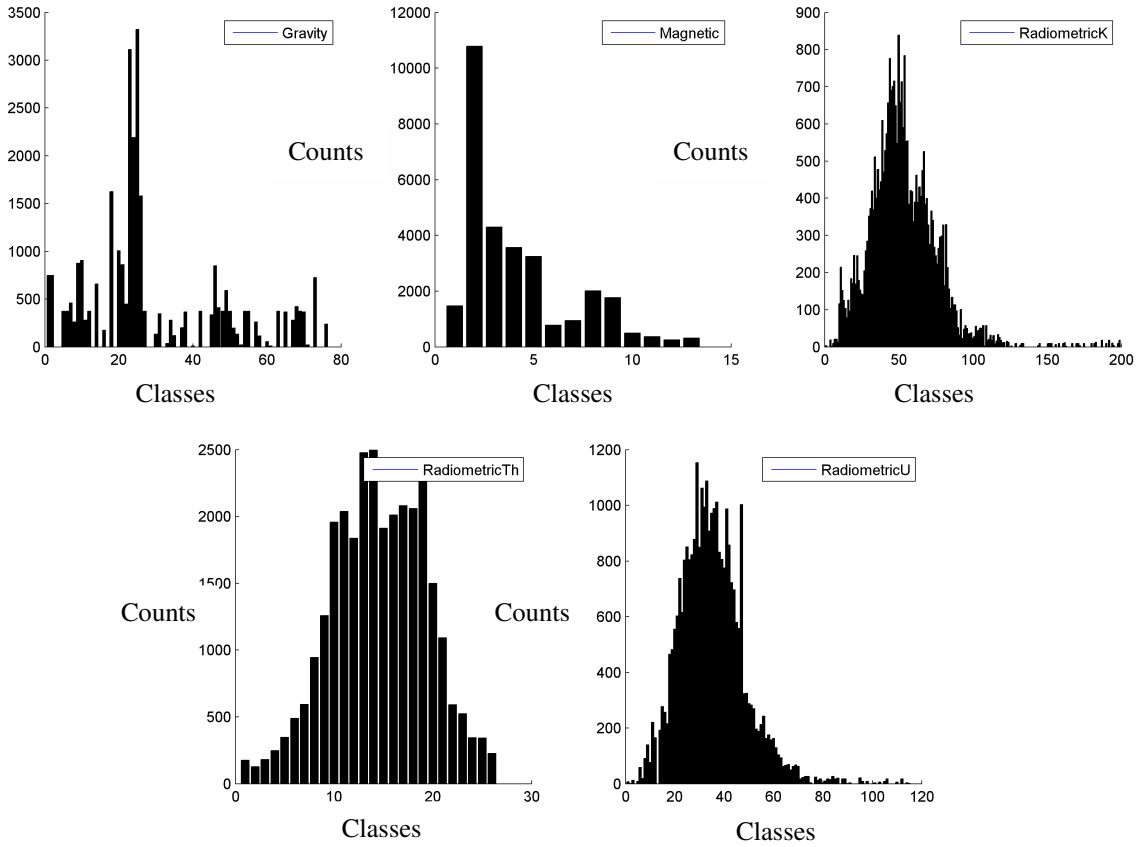

Fig. 3.15 Histograms obtained from Boolean intersection of multiclass geophysical layers. These were used to select the centre of each buffer. Buffer's centres correspond to peaks of correlation and were subsequently used as a starting point for contrast analysis based on cumulative buffering, which was used to select an appropriate buffer size. Gravity and Magnetics datasets have multimodal distributions; therefore, they were subdivided in multiple binary files before contrasting them against the mineral deposit layer.

3.5.2.3. Classification results and ranking

The results of the classification of evidential layers are summarised in Tables 3.2, 3.3, and 3.4. Contrast calculations for the geology were computed over binary layers representing 10 units out of the 36 considered in the previous KD model. This simplification was based on grouping of individual lithostratigraphic units into respective geological formations. Only four units have a studentised C above 1.5 (Pmh, Pa, Pmw, Pmp) and only 3 above 1.95 (Pmh, Pa, Pmw). 1.5 was considered as quality limit for the

Contrast estimation following the recommendation of Bonham-Charter (1994). Contrast results were interpreted considering the error involved in the estimation of the weights, which was calculated following the assumption of asymptotic theory of Bishop et al. (1975), for example Agterberg et al. (1990).

Table 3.2 Weights of evidence computed considering the intersection of deposit area *A(D)* with each geological unit area *A(P)* and relative variances s(W), Contrast (C), and studentised Contrast (Cw) for grouped, lithostratigraphic formations outcropping in the Lawn Hill Region.

Lithostrat.	*A(D)*	*A(P)*	*A(D)/A(P)*	W^+	W^-	$s(W^+)$	$s(W^-)$	*C*	C_w
pmh	17	1121	0.015	2.196	-0.211	0.244	0.124	2.407	8.784
pa	3	230	0.011	1.863	-0.027	0.634	0.112	1.890	2.936
pmw	3	429	0.006	1.270	-0.023	0.622	0.113	1.293	2.047
pmp	1	175	0.008	1.572	-0.014	0.838	0.112	1.586	1.877
pmz	2	763	0.003	0.535	-0.012	0.671	0.112	0.546	0.804
pmr	3	1554	0.002	0.148	-0.005	0.570	0.113	0.153	0.264
pmx	1	678	0.002	0.200	-0.003	0.840	0.112	0.204	0.240
pmt	3	2635	0.001	-0.497	0.023	0.603	0.113	-0.520	-0.847
pml	2	2331	0.001	-0.821	0.028	0.754	0.112	-0.850	-1.114
pms	1	1908	0.000	-1.374	0.031	1.099	0.111	-1.405	-1.272
Tot.	36	11847		0.555	-0.282	0.168	0.147	0.837	3.743
Miss. Ev.	46	35796		-0.282	0.555	0.147	0.168	-0.837	-3.743

The highest number of occurrences is found in the Pmh formation. Other units have one order of magnitude less occurrences, between 1 and 3. Contrast values obtained are also reflected in the ratios of deposit area versus pattern's area (*A(D)/A(P)*, cfr. Tab. 3.2).

The scale of variation of negative weights is indicative of the limited outcrop (small pattern areas compared to total regional area). Additionally, 36 occurrences of 82 are included in known Mesoproterozoic outcrop, whereas the remaining 46 occurrences are proximal to outcropping lithologies, but they are found under Palaeozoic cover sediments

unrelated to mineralisation. To address this issue the cover was considered as missing evidence (see below).

Table 3.3 illustrates the results relative to the Contrast analysis of the structural evidence layers. Contrast and studentised Contrast values were used to order the structural patterns as follow: (1) NE faults, which have the higher degree of spatial association with deposits, with a maximum of 45 deposits/prospects within a 500 m buffer. Then following patterns are; (2) NW faults; (3) fault intersections; (4) E-W faults; and (5) maximum-curvature (fault bends). Although fault intersections have higher Contrast compared to NE faults ($C_{intersections}$ = 2.513 vs. C_{NE} = 2.253), the relative variation of C_w is indicative for the intersection layer of more robustness with a larger buffer of 1000 m. This reduces the C value to 2.121. Therefore, NE faults were considered more important than intersections. This consideration is based also on the total number of occurrences that for equal buffer size, appear to be greater in the NE layer with 55 deposits/prospects in the first 250 m. The fault intersections layer reach 53 deposits only at 1500 m buffer. Comparing the different orientations of faults, note that correlation for NE and NW faults is similar. In Contrast, E-W fault buffers contain markedly lower deposits and maximization of the C is reached at 1750 m instead of 500 m. Comparison of curvature versus intersections indicates that fault intersections have greater potential than bends - this is confirmed at all buffers by deposit number and a C value of 2.207 at highest $C_{w,}$ against a C of 1.055 for the maximum-curvature. All the structural criteria considered demonstrated a strong positive degree of spatial association, suggesting that the structural component is a predominant variable in the Lawn Hill

Region. This would be expected if all the deposits/prospects are fault-hosted examples of vein/lode type.

Gravimetric and magnetic datasets display multimodal distributions - respectively, four and two classes of correlation were defined simplifying original multiclass rasters. Multimodal layers were subdivided in multiple binary rasters representing individual classes of positive correlation. Gravimetric data have the greatest spatial association with deposits/prospects among all geophysical layers. The class Gravity-65 (-892.7 milligals) has the highest value of Contrast and the top value for C and Cw is reached with a buffer between -936.4 and -849.0 milligals intersecting 30 occurrences (Tab. 3.4). Only class Gravity-50 (-1220.4 milligals) other than class Gravity-65 records a studentised Contrast above 1.95 with 12 deposits at maximum C and Cw values. Classes Gravity-86 (-433.8 milligals) and Gravity-113 (156.1 milligals) have lower degree of spatial correlation, and an increasing cumulative buffer results in negative values of Contrast, which indicates negative correlation. These latter two classes appear to be of negligible importance as they never exceed a C_w of 1.95 and buffering never includes more than 10 occurrences within considered ranges of maximization of C. Only initial spikes (see Tab. 3.4 - narrow buffers), are observed in the tabled values for C with relatively large s(C) suggesting inaccurate estimations.

Table 3.3 Weights (W), contrast (C) and relative studentised values (Cw) for cumulative distances from linear and point patterns (fault traces, fault intersections and maximum fault curvature). A(D) deposits area in unit cells, A(P) cumulative buffer areas.

Buffer Dist. (m)	*A(D)*	*A(P)*	*A(D)/A(P)*	W^+	W^-	$s(W^+)$	$s(W^-)$	*C*	C_w
NE faults:									
≤250	55	8045	0.007	1.801	-0.452	0.174	0.144	2.253	9.969
≤500	59	12296	0.005	1.397	-0.952	0.135	0.195	2.349	9.896
≤750	64	16125	0.004	1.040	-1.004	0.130	0.212	2.044	8.213
≤1000	68	19491	0.003	0.845	-1.131	0.125	0.239	1.976	7.315
≤1250	70	22375	0.003	0.706	-1.233	0.122	0.267	1.940	6.617
>1250	82	47643		0.000		0.111			
NW faults:									
≤250	38	5008	0.008	1.594	-0.187	0.246	0.124	1.780	6.469
≤500	45	7854	0.006	1.493	-0.515	0.163	0.151	2.008	9.031
≤750	52	10638	0.005	1.221	-0.634	0.149	0.166	1.854	8.313
≤1000	59	13268	0.004	1.050	-0.759	0.139	0.184	1.810	7.859
≤1250	60	15767	0.004	0.949	-0.939	0.131	0.208	1.888	7.675
≤1500	62	18024	0.003	0.804	-0.937	0.129	0.216	1.741	6.915
>1500	82	47643		0.000		0.111			
E-W faults:									
≤250	9	1258	0.007	1.822	-0.050	0.465	0.114	1.872	3.906
≤500	15	2125	0.007	1.384	-0.084	0.343	0.117	1.468	4.051
≤750	22	3051	0.007	1.412	-0.156	0.260	0.122	1.567	5.450
≤1000	27	4008	0.007	1.462	-0.255	0.212	0.130	1.717	6.906
≤1250	36	5012	0.007	1.383	-0.318	0.192	0.136	1.701	7.229
≤1500	43	6014	0.007	1.431	-0.465	0.168	0.148	1.896	8.480
≤1750	44	7026	0.006	1.426	-0.605	0.154	0.160	2.031	9.148
≤2000	47	8039	0.006	1.305	-0.620	0.151	0.163	1.925	8.653
≤2250	49	9056	0.005	1.234	-0.677	0.146	0.170	1.911	8.518
>2250	82	47643		0.000		0.111			
Fault intersections:									
≤250	18	1182	0.015	2.479	-0.033	0.592	0.113	2.513	4.169
≤500	29	2792	0.011	2.179	-0.219	0.240	0.125	2.398	8.871
≤750	39	4773	0.008	1.822	-0.385	0.186	0.138	2.207	9.534
≤1000	45	6973	0.006	1.573	-0.548	0.160	0.153	2.121	9.552
≤1250	48	9296	0.005	1.321	-0.631	0.150	0.164	1.952	8.768
≤1500	53	11624	0.005	1.115	-0.682	0.144	0.173	1.797	7.967
>1500	82	47643		0.000		0.111			

Buffer Dist. (m)	A(D)	A(P)	A(D)/A(P)	W^+	W^-	$s(W^+)$	$s(W^-)$	C	C_w
Fault max-curvature:									
≤250	6	1188	0.005	1.900	-0.016	0.813	0.112	1.917	2.336
≤500	12	3065	0.004	1.033	-0.047	0.420	0.115	1.080	2.481
≤750	19	5497	0.004	0.838	-0.094	0.288	0.120	0.933	2.992
≤1000	26	8224	0.003	0.718	-0.147	0.228	0.127	0.865	3.316
≤1250	34	11099	0.003	0.610	-0.192	0.197	0.134	0.802	3.368
≤1500	44	13942	0.003	0.586	-0.276	0.171	0.145	0.862	3.839
≤1750	48	16692	0.003	0.619	-0.437	0.150	0.164	1.055	4.746
≤2000	53	19300	0.003	0.519	-0.456	0.145	0.172	0.975	4.333
≤2250	57	21712	0.003	0.465	-0.515	0.138	0.186	0.980	4.237
≤2500	63	23898	0.003	0.418	-0.570	0.133	0.199	0.988	4.121
>2500	82	47643		0.000		0.111			

Table 3.4 Summary of contrast analyses for considered sub-classes of geophysical datasets.

Buffer Property	*A(D)*	*A(P)*	*A(D)/A(P)*	W^+	W^-	$s(W^+)$	$s(W^-)$	*C*	C_w
Gravity 50:	12	3056	0.004	0.981	-0.095	0.299	0.119	1.076	3.346
Gravity 65:	30	2653	0.011	2.143	-0.387	0.189	0.137	2.530	10.838
Gravity 86:	4	1917	0.002	0.617	-0.012	0.681	0.112	0.629	0.911
Gravity 113:	2	1063	0.002	1.158	-0.017	0.719	0.112	1.175	1.616
Potassium 56:	57	16513	0.003	0.716	-0.716	0.135	0.193	1.432	6.072
Thorium 17:	61	28001	0.002	0.201	-0.265	0.140	0.181	0.466	2.037
Uranium 48:	67	32416	0.002	0.205	-0.533	0.124	0.243	0.738	2.705
Magnetic 42:	45	17234	0.003	1.105	-0.313	0.186	0.138	1.418	6.121
Magnetic 48:	78	26348	0.003	0.316	-0.335	0.144	0.174	0.651	2.886

Magnetic classes demonstrate higher correlation to the number of deposits compared to Gravimetric classes; they are also represented by buffers that cover a more extensive area causing a substantial decrease of C, lowering therefore their overall impact on the mineral potential. Among Magnetic classes, Magnetic-42 (-777.1 nanoTesla) has stronger positive correlation, with a relatively narrow buffer. The maximum for C and Cw is respectively 1.418 and 6.121. Magnetic-48 (-452.9 nanoTesla) reaches a maximum value

for C of 0.404 within the first buffer, and then progressively decreases until it finds a strong positive correlation that is derived from the influence of class 42. This trend coupled with a lower Contrast value suggests that class 48 has lower degree of spatial correlation.

In contrast with magnetic and gravimetric datasets, radiometric layers (U-Th-K) are all unimodal and approximately of normal distributions. All classes have Contrast value C that never exceeds 1.5. The K class (1.5 cps) shows the highest positive association. A maximum for C of 1.432 is reached at C_w of 6.072. Despite the elevated number of deposits intersected by Th (11.0 cps) and U (22.6 cps) buffers at maximised C_w, these patterns show larger area compared to the K layer, and consequently lower Contrast. However, the U layer was considered in the Bayesian model due to its strong association to organic-rich lithologies and its value of maximum C_w of 2.705, which is above the 1.5 limit of robustness.

A summary of the evidential layers with C_w above a cut-off of 1.5 is presented in Table 3.5. This includes the Weights of Evidence (W^+, W^-) and relative variances s($W^{\pm}$), the number of deposits/prospects A(D) in overlap with the considered pattern A(P), and relative ratio A(D)/A(P), the calculated Contrast (C), and its studentised value (C_w). Tabulated data were ranked by C to evaluate which layers display the strongest spatial relationship with deposits and prospects. C ranges from 2.530 to 0.738, with all layers demonstrating a positive spatial association. The highest value for the Contrast corresponds to the class Gravity-65 although the Pmh lithotype class has stronger positive correlation (W^+) and higher A(D)/A(P) ratio. The variance of positive weights exceeds 0.2 on the geological map layers; this is due to their size, as they have small areas

intersecting only a small number of occurrences (see Carranza, 2004). Grouping of lithological sub-units was adopted to minimise this type of error. Grouping layers increases the nominal area for a certain lithostratigraphic unit reducing the error on the estimation of the weights $s(W^k)$. Appendix B shows the equation utilised to calculate the standard deviation of the weights following asymptotic assumptions of Bishop et al. (1975). The final layers will be integrated using the Bayes methodology presented in the next section.

Table 3.5 Predictor binary patterns and relative Weights of Evidence, variances and area proportions ranked by contrast (C).

Buffer Class	*A(D)*	*A(P)*	*A(D)/A(P)*	W^+	W^-	$s(W^+)$	$s(W^-)$	*C*	C_w
Gravity 65	30	2653	0.011	2.143	-0.387	0.189	0.137	2.530	10.838
pmh	17	1121	0.015	2.196	-0.211	0.244	0.124	2.407	8.784
NE	54	7453	0.007	1.483	-0.890	0.138	0.187	2.373	10.213
Intersection	38	4593	0.008	1.648	-0.497	0.167	0.148	2.146	9.608
E-W	43	6221	0.007	1.429	-0.603	0.154	0.160	2.032	9.154
NW	38	5082	0.008	1.505	-0.504	0.164	0.150	2.009	9.024
pa	3	230	0.011	1.863	-0.027	0.634	0.112	1.890	2.936
pmp	1	175	0.008	1.572	-0.014	0.838	0.112	1.586	1.877
Potassium 56	57	16513	0.003	0.716	-0.716	0.135	0.193	1.432	6.072
Magnetic 42	45	17234	0.003	1.105	-0.313	0.186	0.138	1.418	6.121
pmw	3	429	0.006	1.270	-0.023	0.622	0.113	1.293	2.047
Gravity 50	12	3056	0.004	0.981	-0.095	0.299	0.119	1.076	3.346
max-curvature	46	15168	0.003	0.601	-0.447	0.149	0.166	1.048	4.702
Uranium 48	67	32416	0.002	0.205	-0.533	0.124	0.243	0.738	2.705

3.5.2.4. Bayesian analysis

The Bayesian rule of combination assumes a conditional independence (CI) between evidential layers (Bonham-Carter, 1994). This condition is posed to avoid the overestimation of posterior probabilities, which often requires rejection of some evidence.

3.5.2.4.1. Set theory

The most intuitive way to describe the Bayesian method of data aggregation is using the Venn notation (Bonham-Carter, 1994; Carranza and Hale, 2000). Fig. 3.16 portrays an example of Venn diagrams that describes the spatial associations between different variables. Areas of overlap of evidential layers within Venn diagrams define a series of positive and negative spatial associations. Intersections can be thought of as a graphical representation of the degree of spatial association between multiple datasets.

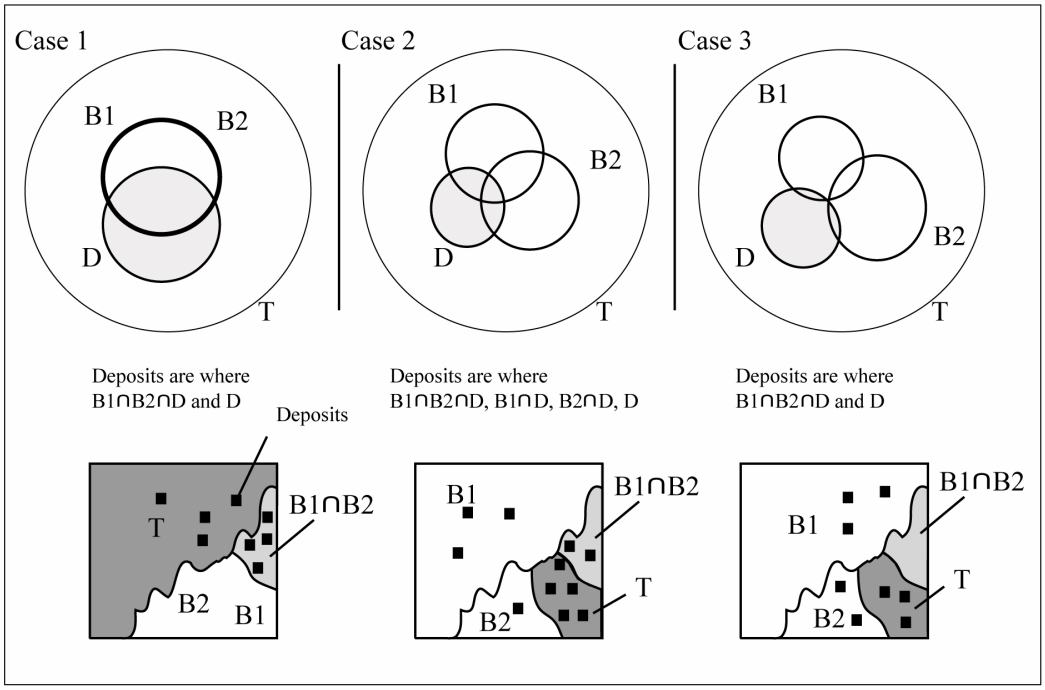

Fig. 3.16 Venn diagrams and schematic plan views representing different conditions of overlap among binary layers. Application of the Bayes rule can lead to overestimation as a function of the type of overlap among patterns and deposit areas. Case 1 shows that if B1=B2 then CI is always violated (see text). Case 2 is the most common example in which CI may be respected or not depending upon the area proportions. Case 3 always violates the conditional independence assumption as double intersection has always value equal to zero; whereas, single intersections are positive (area >0). However, this type of violation is unlikely as patterns are usually chosen maximising spatial correlation to mineral deposits.

3.5.2.4.2. Definition of P_{prior} and P_{post}

Usually in mineral potential mapping, a prior probability (P_{prior}) is defined dividing the total area of known mineral occurrences N(D) by the total area of a selected region N(T) containing the mineral deposits/prospects (both terms are expressed in unit cell), P_{prior} = N(D)/N(T). P_{prior} represents the likelihood of finding a mineral deposit in the selected region, estimated using the spatial knowledge of known occurrences. Conventionally every known mineral deposit/prospect occupies a small unit cell area (pixel) (Agterberg et al., 1990), to minimise the errors of estimation s(W^k) respecting the asymptotic theory assumptions (see Appendix B). Consideration of additional themes, for example the NW faults which appear associated with an elevated number of prospects, is a bias for the P_{prior}. New deposits/prospects are expected to be discovered where other NW faults intersect the study area. However, other variables may have influenced the spatial distribution of known deposits. All evidential themes (B_1, B_2, B_n…B_{n+1}) are weighted against the mineral deposit layer (D). Positive and negative spatial association is expressed in 2D-GIS as a probability surface. Therefore, a posterior probability (P_{post}) can be defined as the product of P_{prior} with a series of factors representing updating functions, based on the new knowledge of spatial association.

Probability in WofE is represented as Odds (see Appendix B for equations). Odds are also expressed in logarithmic form obtaining a representation of the probability as pri- and postlogit that favours integration (see Appendix B), because simple addition of weights to the prilogit allows combination of evidence (Spiegelhalter, 1986; Bonham-Carter, 1994). This approach can be defined as the Bayes rule of combination.

3.5.2.5. Conditional independence testing

3.5.2.5.1. Meaning of conditional independence

As previously introduced, a Bayesian model is based on the assumption that conditional independence (CI) between overlapping patterns is unviolated. The model assumes that calculated Weights of Evidence must be derived from patterns that are independent of one another. Thiart et al. (2003) remark that it is unlikely that such conditions will be fulfilled when overlapping multiple themes. It is natural then to raise questions regarding the extent of violation and also to define where such violations occur to understand where the probabilistic model is responding with overestimation. Therefore, to quantify and qualify CI, multivariate statistical tests commonly used to define the interval of confidence were adapted to mineral potential applications (e.g. G^2, see Agterberg et. al., 1989; χ^2, Bonham-carter, 1994; OT and New OT, Agterberg and Cheng, 2002, and Carranza, 2004). The CI assumption can be algebraically defined, for a two-layer model, as:

$$P\left(B1 \cap B2|D\right) = P\left(B1 \cap D\right) P\left(B2 \cap D\right) \tag{3.1}$$

This equation states that the joint probability $P(B1 \cap B2 \mid D)$ of finding a mineral deposit (D) at the intersection of two patterns ($B1$, $B2$) must be equal to the product of the independent probabilities of finding occurrences within $B1$ and $B2$. Areas of intersection

vary as a function of selected patterns and, as a consequence, the above relationship can be either satisfied or not.

3.5.2.5.2 Graphic approach to understand CI

To better define the significance of the CI assumption an example is proposed that considers two patterns that exactly coincide, i.e. *B1 = B2* (Fig. 3.16, case 1). Being equal patterns the two layers have analogous spatial association with the mineral deposits and therefore equal weights (W^k). Assuming that the mineral deposit areas are relatively small, then the posterior probability resulting from the doubling of patterns *B1* and *B2* will be e^2, which is 7.4 times larger than if the two layers are conditionally independent (Agterberg and Cheng, 2002). A comparison between different types of intersections is presented in Fig. 3.19. The previous example, adapted from Agterberg and Cheng (2002), represents an end-member condition (Case 1) in which CI is always violated as the double intersection $B1 \cap B2 \cap D$ is equal to $B1 \cap D$ and $B2 \cap D$. The Case 2, adapted from Bonham-Carter (1994), is a more generalised example of pattern overlap that can lead either to violation or non-violation of conditional independence. Case 3 represents the counterpart to Case 1 and has zero probability of finding a mineral occurrence where B1 and B2 intersect one another. However, both patterns show spatial association with mineral deposits. Case 3 leads to CI violation. This consideration suggests that violation of CI might occur also when patterns tend to overlap without having equal spatial association with mineral deposits. However, the latter example is rare as evidential layers are chosen and standardised aiming at maximizing correlation. The Illustrated examples suggest that CI will be violated more likely if proximal to end-member conditions (Case

1 and Case 3), which means when the areas of intersection $B1 \cap D$, $B2 \cap D$ and $B1 \cap B2 \cap D$ are equal or tend to zero.

3.5.2.5.3 CI tests

Overestimation of posterior probability due to CI violations is reduced in different ways; the simplest approach is to reject evidential themes that cause CI violation (e.g. Thiart et al., 2003). However, in some cases (e.g. considering geochemical patterns) it is convenient to merge problematic themes using logistic regression or principal component analysis (Agterberg, 1992; Carranza, 2004).

CI violation can be assessed using goodness of fit tests (e.g. Bishop et al. 1975), or alternatively using overall calculations of posterior probability. Both approaches can be used to identify which layers induce violation although the latter allows testing of multiple layers, reducing the number of iterations required to identify problematic patterns.

The first approach makes use of Pearsonian statistics (Chi-square) (see Bonham-Carter, 1994) or likelihood-ratio statistics (G^2 e.g. Bonham-Carter et al., 1989) that can be used for multinomial or Poisson distributions (Bishop et al., 1975). These tests are commonly pairwise and run on fourfold tables constructed to attribute a structure to the data. Tests for the goodness of fit are limited to areas intersecting deposits in mineral potential applications (Fig. 3.17). The probability of occurrence in a certain cell is indexed by two characteristic variables (i, j) that define its dependency from chosen parameters. In addition to internal probabilities, marginal unconditional probabilities are calculated to obtain maximum likelihood estimates. It is of particular interest to explore

the difference existing between internal and external (marginal) probabilities in a fourfold table, to evaluate spatial association. Two equations are commonly used to calculate respectively Chi- and *G*-square statistics:

$$\chi^2 = \sum_{i=n}^{n} \frac{\left(O_i - E_i\right)^2}{E_i} \tag{3.2}$$

$$G^2 = \sum_{i=n}^{n} x_i \ln\left(\frac{\hat{m}_i}{x_i}\right) \tag{3.3}$$

The first represents the summation of the squared differences between expected (*Ei*) and observed (O_i) frequencies of unit cells (n). *G*-square is distributed as χ^2 with 2 degrees of freedom (Bishop et al., 1975) with $\hat{m}$ representing the predicted area versus observed area in unit cells. If $\hat{m}$ differs strongly from x, the test fails. Both methods consider a centred sampling distribution to fulfil the null hypothesis (H_0); therefore, Chi- or *G*-square estimates tend to zero when there is no difference among patterns. Commonly a p-value (alpha) is defined choosing an interval of confidence (e.g. 95%). If the calculated p-value is less than the chosen value the test is rejected. The chosen p-value corresponds to the value limit for acceptance of Chi- or G-square results. Statistical tables are available for comparison. Tabulated values are ordered by chosen alpha, but also they vary as a function of the degree of freedom (*df*), which is the number of parameters that may be independently varied. *df* is then function of the number of evidential layers, but also the number of classes within a single theme contributes augmenting its value. For example, the *df* is calculated for a 2x2x2 table as follow:

$$df = (n - classes\ within\ theme\ B1 - 1) \times (n - classes\ within\ theme\ B2 - 1) \tag{3.4}$$

Results of Chi- or G-square statistics have to be carefully evaluated. Here I briefly discuss the problem relative to the Chi-square analysis as this approach was preferred and implemented in the WofE modeller considering the examples proposed in Bonham-Carter (1994). The software is capable of choosing automatically all the possible n-pairs of evidence and calculating multiple Chi-square values based on the fourfold table previously introduced (Fig. 3.17). Note that several limitations apply to this methodology and this test cannot be considered statistically robust (Bonham-Carter, 1994). Chi-square results should be considered in relationship to others and not in an absolute sense; this is due to their dependency from the area of study, and also from the resulting area of intersection among patterns and deposit layers. Area dependency for example means that having a limited number of deposits may induce erroneous results because of low expected frequencies in the contingency table (Snedecor and Cochran, 1967; Bonham-Carter, 1994; Carranza, 2002). This is mainly due to the limit conditions of the asymptotic result commonly used in case of finite random variables (Bishop et al., 1975). In a mineral potential example if the number of samples (deposits) is small and resulting prior probability is close to 0, the approximation is poor. It is possible then to apply the Yates correction (see following equation) inducing a reduction of the final Chi-square values; however, the correction cannot be applied if the absolute value of the difference between observed and expected counts is lower than 0.5 (Bonham-Carter, 1994). In any case if the expected value in any cell is less than 5, the Chi-square results are inaccurate.

More empirical estimations such as the Overall test (Bonham-Carter, 1994) and the New Omnibus Test (Agterberg and Cheng, 2002; Thiart et al., 2003; Carranza, 2004)

were integrated in the WofE modeller to offer an alternative to pairwise Chi-square tests. The main reason for relying on multiple tests is that they offer a comprehensive evaluation of conditional independence and help substantially when recombination or rejection of evidence is required. Overall tests can be applied after Bayesian combination, over multiple layers. Experimental results presented in the next session suggest that CI is not only a function of the overlapping conditions occurring among positive patterns (as assumed in pairwise Chi-square testing), leading in several cases to discrepancies between Chi-square results and overall tests. Therefore, assessment of CI with different methodologies is considered essential to the more complex cases involving a large number of evidential layers such as the application presented below, with a total of 14 themes. Two linear equations that reflect sums of post-probability summarise the methodology and logic of these tests:

$$N(D)_{Pred} = \sum_{k=n}^{n} \left(P_k \, N(k) \right) \tag{3.5}$$

$$NOT = \frac{N(D)_{Pred} - N(D)}{s\left(N(D)_{Pred}\right)} \tag{3.6}$$

These kernel algorithms simply compare the number of known deposits $N(D)$ in a certain region (P_{prior}) with the number of predicted mineral deposits or prospects $N(D)_{\text{Pred}}$ obtained from (P_{post}) overall values. A posterior probability map can be imagined in 3D as composed of columns of pixels (unit cells) that carry different weights depending upon their spatial location (Fig. 3.18). Each column is part of a certain class (i) of pixel columns with a total posterior probability (P_k). Each class (k) has a certain size defined

by the area of occupancy expressed as pixel number $N(k)$. The overall posterior probability (number of predicted deposits) can be estimated summing up the products of all known classes k_n for their respective n-pixels of occupancy. The total posterior probability can be converted back to a hypothetical number of deposits multiplying by the overall P_{post} for the total number of unit cells $N(T)$. Bonham-Carter (1994) firstly adopted this methodology suggesting that a cut-off of 10-15% (OT value of 0.85) has to be considered as a limit for violation. In other words, CI is violated when predicted deposits are 10-15% more than known occurrences, and OT results are lower than 0.85. There is however uncertainty regarding the imposed limit that is set purely on an empirical base and may be too conservative (Thiart et al., 2003). In fact, lower limits might still be acceptable if comparing results from WofE with Logistic Regression analysis (Thiart et al., 2003). Similar results are illustrated in the following application where excessive OT conservativity was revealed by comparing OT with NOT results.

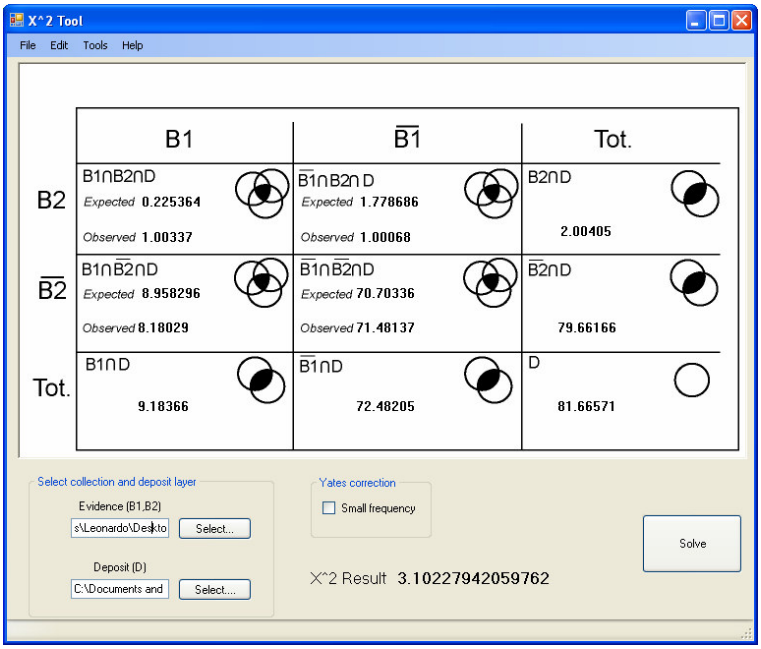

Fig. 3.17 Example of χ^2 output of the WofE modeller (Appendix E) showing a contingency table in which partial output of the χ^2 analysis can be assessed to allow application of Yates correction if required (see Bonham-Carter, 1994). The overall $\chi 2$ value is also computed and displayed, additionally a *.txt file is saved if multiple layers are considered rather than just a binary couple (B1, B2).

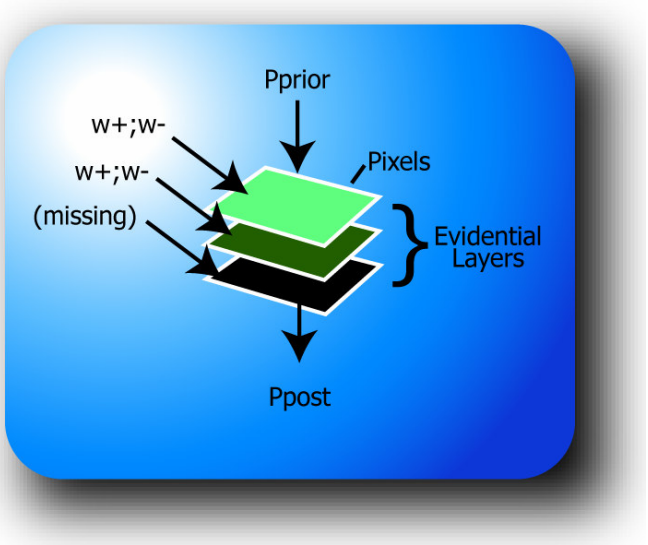

Fig. 3.18 Diagram portraying Bayesian combination of multiple evidential layers. Each evidential layer is composed of n-pixels. These can be imagined as part of columns of multiple n-pixels in case of multiple layers. n-columns correspond to n-combinations of n-weights and or missing information. Sum of evidence in each pixel column can be seen as an overlap relationship in which initial Pprior is updated to give a final Ppost.

To refine the results of the OT test Agterberg et al. (1993) has applied the Kolmogorov-Smirnov statistic for the goodness-of-fit assuming that the P_{post} distribution approximates normality. This test fits the observed P_{post} distribution to a cumulative curve representing a normal distribution. Usually P_{post} are firstly divided by the total number of known occurrences D, and afterwards are plotted within a confidence envelope. If observed P_{post} /D values exceed this interval the test fails (e.g. Agterberg and Cheng, 2002, Bonham-Carter et al., 1989). The validity of this test for mineral potential mapping applications is briefly discussed in Agterberg and Cheng (2002). Before applying the goodness-of-fit test it is preferable to evaluate the null hypothesis (number of predicted deposits equal to number of known deposits), which is equivalent to the CI hypothesis. In Weights of Evidence modelling the maximum difference is generally expressed as $(N(D)_{\text{Pred}}/N\{D\} - 1)$. Testing in advance the proposition $N(D)_{Pred}=N\{D\}$ would be reducing the maximum difference to zero allowing application of the Kolmogorov-Smirnov statistic. The proposition can be tested statistically as it is possible to calculate the s^2 $(N(D)_{\text{Pred}})$ see Appendix B. Briefly the error estimate of $N(D)_{\text{Pred}}$ is derived from the errors estimated for the Weights of Evidence.

In this context the NOT (New Omnibus Test) represents an improved formulation of the OT test, in which the uncertainty in the estimation of $N(D)_{\text{Pred}}$ is introduced as additional parameter (see equation 3.6). Note that the variance of the posterior probability $s^2(P_{post})$ inherits the asymptotic approximation assumptions as it is based on the variance of the weighs of evidence calculated using the formulas based on asymptotic approximation of Bishop et al. (1975). Therefore, this test is statistically more robust than the OT allowing a better qualification of probability estimates although it is more

effective on large populations. The effect of CI violation induces underestimation of the standard deviation of P_{post} incrementing the NOT result. Therefore, the NOT test is more sensible to CI violation. NOT results approximate a normal distribution that can be used to calculate p-values that are finally compared against a certain confidence interval alpha, as previously seen for the Chi-square tests, although in this latter case a normal distribution is fitted to the data.

3.5.3. Uncertainty from missing evidence

As mentioned an estimate of the error involved in the calculation of P_{post} is available $s(P_{post})$. This parameter depends upon the uncertainty of information gathered. When information is lacking, for certain areas, and in some if not all evidential layers, then uncertainty of P_{post} will be higher compared to unit cells where information is complete for all patterns. To account for missing patterns the methodology of Agterberg et al. (1990) was implemented in the WofE modeller. Mathematically, ignorance is expressed considering any P_{prior} as an expectation function (Ex) of P_{post}. In other words, P_{prior} may be closely matching P_{post} and the certainty regarding this hypothesis (expectation) is function of the amount of available evidence $P(x)$ that may support a prior estimate. This concept can be expressed as an iterative sum of evidence:

$$P_{prior} = \int P_{Post} \cdot P(x)\, dx = Ex\left[P_{Post}\right] \tag{3.7}$$

Considering two patterns *(B1, B2)* updating a $P_{prior} = P(D)$ the iteration becomes a finite sum of probabilities multiplied by a weighting coefficient that depends upon their respective area of occupancy expressed as $P(B_i, B_j \ldots B_n)$ and relative intersection with known deposits *D*. The final equation becomes then:

$$P(D) = P\left(D \mid B1, B2\right) \cdot P\left(B1, B2\right) + P\left(D \mid \overline{B1}, B2\right) \cdot P\left(\overline{B1}, B2\right) + \\ + P\left(D \mid B1, \overline{B2}\right) \cdot P\left(B1, \overline{B2}\right) + P\left(D \mid \overline{B1}, \overline{B2}\right) \cdot P\left(\overline{B1}, \overline{B2}\right) \tag{3.8}$$

All possible combinations of *B1* with *B2* update the P_{prior} in a different manner. The relative uncertainty involved in this calculation, in case of a single missing evidence layer, can be defined as the sum of the square difference between P_{post} calculated without missing evidence and P_{post} calculated for missing evidence. For one layer of missing information P_{post} becomes P_{prior}. The variance $s_m^2(P_{post})$ is obtained then by summing up these partial variances weighted by their relative area proportions, similarly to the expectation function:

$$s_m^2\left(P_{Post}\right) = \left[P\left(D \mid B1\right) - P(D)\right]^2 \cdot P(B1) + \left[P\left(D \mid \overline{B1}\right) - P(D)\right]^2 \cdot P\left(\overline{B1}\right) \tag{3.9}$$

A numerical example of its application is found in Carranza (2004). Missing patterns affect the calculation of P_{post}, not only its variance (Appendix B for equation). The results obtained can be used to map the spatial distribution of uncertainty across the study area; however, this tends to resemble the overall pattern of P_{post} (Agterberg et al. 1990).

Once the calculation of the error involved with missing patterns is completed, its value is simply added to the error derived from the calculation of weights (W^+, W^-). Both terms are calculated on a pixel (unit cell) base, and their overall sum is obtained and imputed in equation (3.6) for NOT calculation.

There is then a double component of error involved in the estimation of P_{post} that is a function of uncertainty in the value of P_{post} due to missing evidence and also an error due to the asymptotic approximation adopted. Limits of this methodology are remarked in Bishop et al. (1975, Chapter 14). A way to improve P_{post} calculation might be to consider, similarly to what Agterberg et al. (1989) suggest, a map that represents the ratio between P_{post} and $s(P_{post})$. The methodology of rejection could be then based on the rejection of pixel columns (rather than entire layers of information) tested in term of both uncertainty of estimation and also CI violation.

3.6. Pb-Zn mineral potential for the Lawn Hill Region

The final outcome of the posterior probability analysis is a map composed of evidential themes that passed CI tests for conditional independence. A reduction from fourteen to eleven layers was required to ensure CI acceptance under described statistical tests. However, to obtain such results a multiple testing procedure was established because the number of layers was large. With multiple layers, N^2 combinations are possible (N is the number of layers) although some simplification arise from the problem symmetry, reducing the number to (N^2- $N/2$). Therefore, having an initial number of 14 layers, a total of 91 binary combinations were tested using χ^2 statistics for CI (Fig. 3.19).

One of the advantages of the WofE modeller is its internal algorithm for pairwise combination that automatically determines the N possible couples providing comprehensive Chi-square statistics. A summary of the results is presented in Fig. 3.19; the diagram illustrates the Chi-square output for each possible combination and is ordered as a function of the magnitude of Chi-square values, which is equivalent to the distance from the null hypothesis (H_0). Nine couples were selected for further comparison with OT and NOT tests. Selection criteria aimed to include values that violated CI for the following intervals of confidence: (1) a Chi-square of 5.4 at 98% and (2) a 3.8 value for a confidence interval chosen at 95% of the Chi-square distribution (see Bonham-Carter, 1994; Walker and Lev, 1953). Overall results and chosen couples revealed that:

(1) Approximately 10% of combinations violate the Chi-square test;

(2) only geophysical and structural patterns revealed a CI violation issue; and

(3) multiple pairwise Chi-square comparison can be used to define how much a layer is contributing to CI violation throughout its interrelationship with other themes. Binary themes were ranked using this consideration showing that the intersection layer was the most troubled pattern followed then by northwest oriented faults, gravity-65, magnetic-42, gravity-50 and finally the east-west faults.

In several cases, the frequency for expected values of contingency tables were lower than five (reducing robustness). The Chi-square tests demonstrated a higher sensibility to CI violation if compared to the overall tests. This might be exclusive of the examined area, but more likely was linked to the different approach utilised by these latter methods in assessing CI. Chi-square analysis considers exclusively areas of patterns intersecting

the mineral occurrences layer (D), whereas Omnibus (Overall) tests consider all the unit cells in the model. To further understand this difference, OT and NOT were run on the same combinations identified as violating CI after Chi-square analysis, for comparison (see Tab. 3.6, comparison CHI OT NOT). Results suggest the following considerations: three combinations failed all tests; these include only structural layers (Intersection, NW, NE and E-W). All the other cases failed for Chi-square, but passed both OT and NOT. This discrepancy depends on area proportions and relative pattern overlap. For the Lawn Hill region, the area between any pattern and known occurrences do not exceed a maximum of 8.2 km^2, which is a relatively small area compared to the total area of 4764.2 km^2. Therefore, the number of pixels contributing with negative spatial association (W^-) is always greater than pixels having positive association. Described spatial interactions cause then a reduction of the overall estimation of posterior probability justifying the difference among tests and resulting estimates proximal to 1 for the OT, and 0 for the NOT tests (Tab. 3.7). Note also that failure of OT and NOT is occurring within layers that have the larger areas of positive spatial association (W^+).

Table 3.6 Comparison of CI results of chi-square pairwise evaluation against OT and NewOT tests.

Couples		*χ2*	*χ2 (Yates corr. applied)*	*OT*	*(OT)*	*NOT*	*(NOT)*
Gravity65	Magnetic42	33.290	30.198	1.075	passed	-0.557	passed
Gravity65	Fault intersections	27.267	24.575	0.950	passed	0.365	passed
Gravity65	Northwest faults	23.280	20.805	0.989	passed	0.082	passed
Magnetic42	Fault intersections	12.300	10.722	0.951	passed	0.432	passed
Northwest faults	Fault intersections	10.814	9.394	0.674	failed	2.038	failed
Northwest faults	Magnetic42	9.704	8.312	0.959	passed	0.327	passed
Northwest faults	Gravity50	7.977	6.053	1.041	passed	-0.277	passed
Northeast faults	Fault intersections	6.444	5.314	0.629	failed	2.226	failed
Fault intersections	East west faults	5.436	4.446	0.804	failed	1.421	failed
Magnetic42	Gravity50	5.207	3.621	1.040	passed	-0.263	passed

Table 3.7 Omnibus and New-Omnibus test results for multiple combinations of evidential themes.

Groups	*n-layers*	*OT*	*(OT)*	*NOT*	*p(NOT)*	*(NOT)*
		Missing evidence absent				
Structure	5	0.209	Failed	4.957	0.000	Failed
Geology	4	1.005	Passed	-0.023	0.509	Passed
Geophysics	5	1.108	Passed	-0.920	0.821	Passed
Structure + Geophysics	10	0.174	Failed	11.970	0.000	Failed
Structure + Geology	9	0.192	Failed	5.723	0.000	Failed
Geology + Geophysics	9	0.898	Passed	0.909	0.182	Passed
Total Evidence	14	0.163	Failed	13.831	0.000	Failed
Optimised Evidence	11	0.481	Failed	5.798	0.000	Failed
		Missing evidence present				
Geology	4	0.851	Passed	0.007	0.497	Passed
Structure + Geology	9	0.177	Failed	1.474	0.070	Failed
Geology + Geophysics	9	0.789	Passed	0.037	0.485	Passed
Total Evidence	14	0.153	Failed	6.101	0.000	Failed
Optimised Evidence	11	0.437	Failed	0.460	0.323	Passed

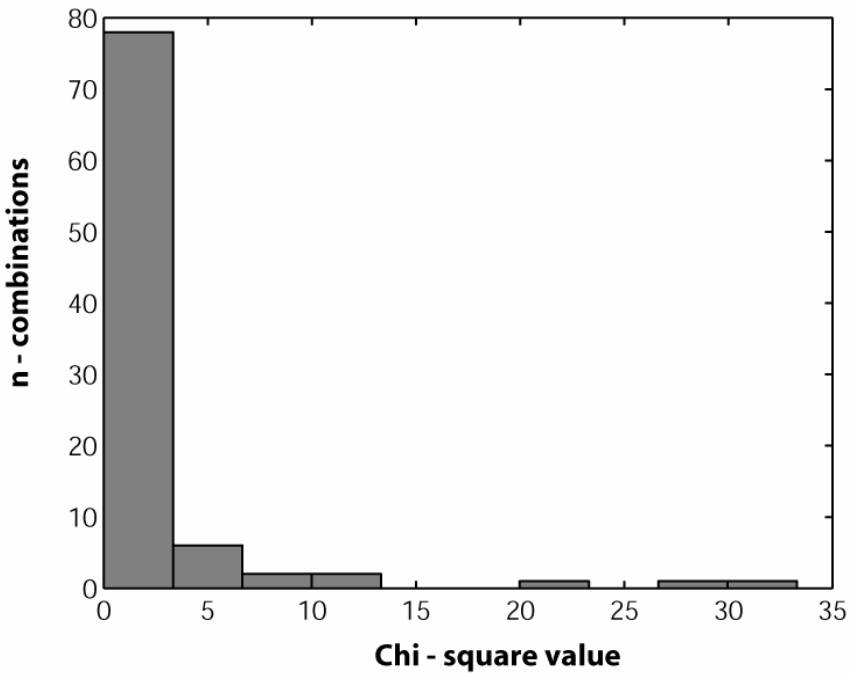

Fig. 3.19 Histogram of 91 pairwise combinations obtained using the WofE modeller (χ^2 tool). Most of the couples pass the χ^2 test at 95% confidence. Couples that violate the χ^2 test were considered in additional CI tests for comparison (see text).

To further validate the mineral potential model, the 14 layers were grouped distinguishing them by type (Structural, Geological, and Geophysical), and running multilayer OT and NOT tests either on separated groups or coupling them (see Tab. 3.7). Outcomes of this analysis include also OT, NOT tests for a full (14 layers) model, and a final optimal combination with 11 layers, rejecting the intersection, curvature and E-W layers to show P_{post} variation during rejection procedure.

Serial rejection tests were carried out firstly evaluating possible internal CI violations within selected groups. Among the 3 multiple sets only the Structure-set failed both overall tests. Geology- and Geophysics-sets passed all overall tests confirming that the Structure-set has the only internal violations of CI. In contrast, the geophysical pattern is showing underestimation of P_{post}, e.g. OT records a value of 1.1 (Tab. 3.7). The observed relation suggests that serial analysis may help revealing CI violation but also can be used to understand why certain combinations tend to smooth CI problems as they reveal underestimation cases in addition to troubled CI layers.

Coupling of groups suggested that CI violation was also occurring among them (e.g. Structure and Geology). In fact, all the combinations including the Structural-set failed both overall tests. When also the Geophysics-Geology combination passed OT and NOT tests, it was concluded that only the Structural group had CI violation issues. Therefore, a rejection of some of the structural layers based on the degree of violation assessed comparing the different tests (Tab. 3.7), led to an optimal model that passed CI tests in the case of missing evidence. As seen in the examples presented in Thiart et al. (2003) and Carranza (2004), consideration of missing patterns tends to increase the number of

predicted mineral deposits/prospects, favouring rejection of OT, but at the same time favouring acceptance of the NOT test (see equation in Appendix B).

The NOT results satisfy the condition imposed by the Weights of Evidence method with a value of 0.460 and p-value of 0.323, which is greater than an alpha of 0.05 at 95% confidence. This result was computed using the WofE modeller, which can treat uncertainty due to missing information during estimation of posterior probabilities and relative standard deviation induced by a missing pattern s_m (P_{post}). The software was also designed to handle multiple missing patterns, to improve multilayer OT and NOT tests. It allows loading one or more binary files representing a missing evidence pattern for each evidence theme considered in the P_{post} model. Integrated patterns are used to update the Weights of Evidence, converting the weights calculated with Contrast analysis to zero if they represent a missing pattern. Additionally, WofE computes the $s_m(P_{post})$ that is added to the error derived from the weights approximation s(W).

The results presented in Table 3. (including the final P_{post} model based on 11 layers), represent examples of OT and NOT variation considering missing patterns. Four missing evidence patterns were considered to account for additional uncertainty within geologic units that were obtained from recombination of twenty lithostratigraphic classes (same classification as KD model above, but simplified into formations, see Fig. 3.3). Areas counted as missing evidence represent Post-Proterozoic cover sediments that might be hiding undercover mineral deposits. This also is an obstacle to the correct assignment of Weights of Evidence and their calculation. Recalculation of post probabilities was then undertaken considering a common missing pattern representing the cover.

Values of OT and NOT (Tab. 3.7) are suggesting, in agreement with the observation of Agterberg and Cheng (2002) and Carranza (2004), that considering missing evidence generally improves the result of overall tests for conditional independence, as indicated by the relative increase of OT and decrease of NOT values. Equation 3.6 expresses dependency of CI violation from two parameters: (1) P_{post} values vary accordingly to weights variation depending on the proportion of pixels converted to zero when missing information is considered; and (2) Number and extent of missing patterns influence the estimation of $s_{Tot}(P_{post})$ as $s_{Tot}(P_{post}) = s(P_{post})+s_m(P_{post})$. In the Lawn Hill region example, the missing patterns occur mostly where weights revealed negative-correlation to mineral deposits/prospects (W^-). If these areas are considered as missing patterns then an increase of the P_{post} is expected due to the omitted effect of negative correlation, which contributes to violation. The OT result fails the test with a higher value, confirming this hypothesis. Nonetheless, the increased uncertainty in the calculation of P_{post} plays an important role controlling the validity of NOT tests. The NOT result revealed that the missing information may be a determinant in reducing violation of CI, in particular for circumstances as shown previously with an 11 layer model. Even though the OT test fails, the model passes the NOT test. Indeed this result is consistent with remarks of Thiart et al. (2003) who compared OT and NOT results. In this regard the more statistical robustness of the NOT test was considered as a guideline to ascertain validity of the mineral potential model. The empirical violation limit of 0.85 for the OT test (Bonham-Carter, 1994) was then considered too conservative.

The eleven layer model is presented in Fig. 3.20a and 3.20b as a final P_{post} map. Probabilities were rescaled using a 256 colour gradient to display their variation; each

value above zero represents a posterior probability greater than the prior probability calculated from the mineral deposit layer. This map was created using a binary converter that creates a bitmap file from a binary array of posterior probabilities using windows GDI+ (Graphic Device Interface Library).

The probabilistic map shows that a limited area (approximately 14.85 %) records a ratio of P_{post} / P_{prior} greater than one, which is favourable for Pb-Zn mineralisation. The probabilistic map compared to known mineral occurrences (Fig. 3.20a) shows also that nearly 70% of the mineral deposits and prospects (57 out of 82) occur within the area considered as having probable potential for Pb-Zn ore. It is interesting to note that this data-driven model has highest values of probability (0.9441) corresponding to the Century zinc deposit. Similar potential is recorded northwest of Century where frequent clusters of mineral deposits and prospects are predominantly hosted in veins and lodes and proximal to northeast trending structures. However, the data-driven model does not discriminate any tonnage for the mineral deposits and it is not differentiating between vein-style mineralisation and stratiform ore deposits similar to Century. The range of probabilities observed can be grouped in low-probability domains (0 to 0.4721) and high-probability domains (0.4721 to 0.9441). Most of the highly predictive domains are focused around the Termite Range Fault and form a broad zone that, as expected, fits known occurrences although adding new potential targets proximal to them (see Fig. 3.20b). It is also interesting to note that intermediate to low-probability targets occur in other peripheral areas. For example, the Kamarga Dome area has small clusters of predictive pixels mostly where faults intersect the Pmx, Pmz and Pmp units. Low-probability domains may be regarded as possible sites of new discovery as the training

sites utilised in this data-driven model had most of the deposits occurring in the High-probability domains. The mineral potential model is also based on a large number of predictive themes; therefore, in some cases some of the low-probability values may be resulting from smoothing of themes that alone might have been suggesting significant mineral potential.

To further validate the mineral potential map a methodology similar to Carranza (2002) was adopted; firstly constructing a geochemical map representing interpolated anomalies of Zn for known stream sediment data and in a second step calculating the percentage of overlap existing among values of P_{post} higher than P_{prior} and Zn anomalies above 100 ppm (stream sediment data were provided by Zinifex Pty. Ltd. Century Mine) (Fig. 3.20b – white highlighted polylines). The outcome suggests a moderate agreement with mineral potential, with 47% overlap. This result could be justified considering that as previously discussed the extent of Post-Proterozoic cover may contribute to underestimation of covered sites. The same argument may be considered to explain also the occurrence of 46 deposits in areas proximal to predictive domains, but recorded outside them. Comparing the deposit theme with the cover theme approximately 50% of the prospects occur in cover sediments or Post-Proterozoic areas mostly proximal to the Mesoproterozoic mineralised outcrops, supporting this argument. In the conclusions, some of these limitations, due to incomplete data and scarce knowledge concerning the mineral deposits/prospects, is addressed integrating data-driven results with the KD-model. However, the constructed mineral potential map passed CI tests for violation of conditional independence and has demonstrated a reasonable agreement with known

deposits and stream sediment data; therefore, it is believed to be a valuable guide to establish new strategic exploration sites in the Lawn Hill Region.

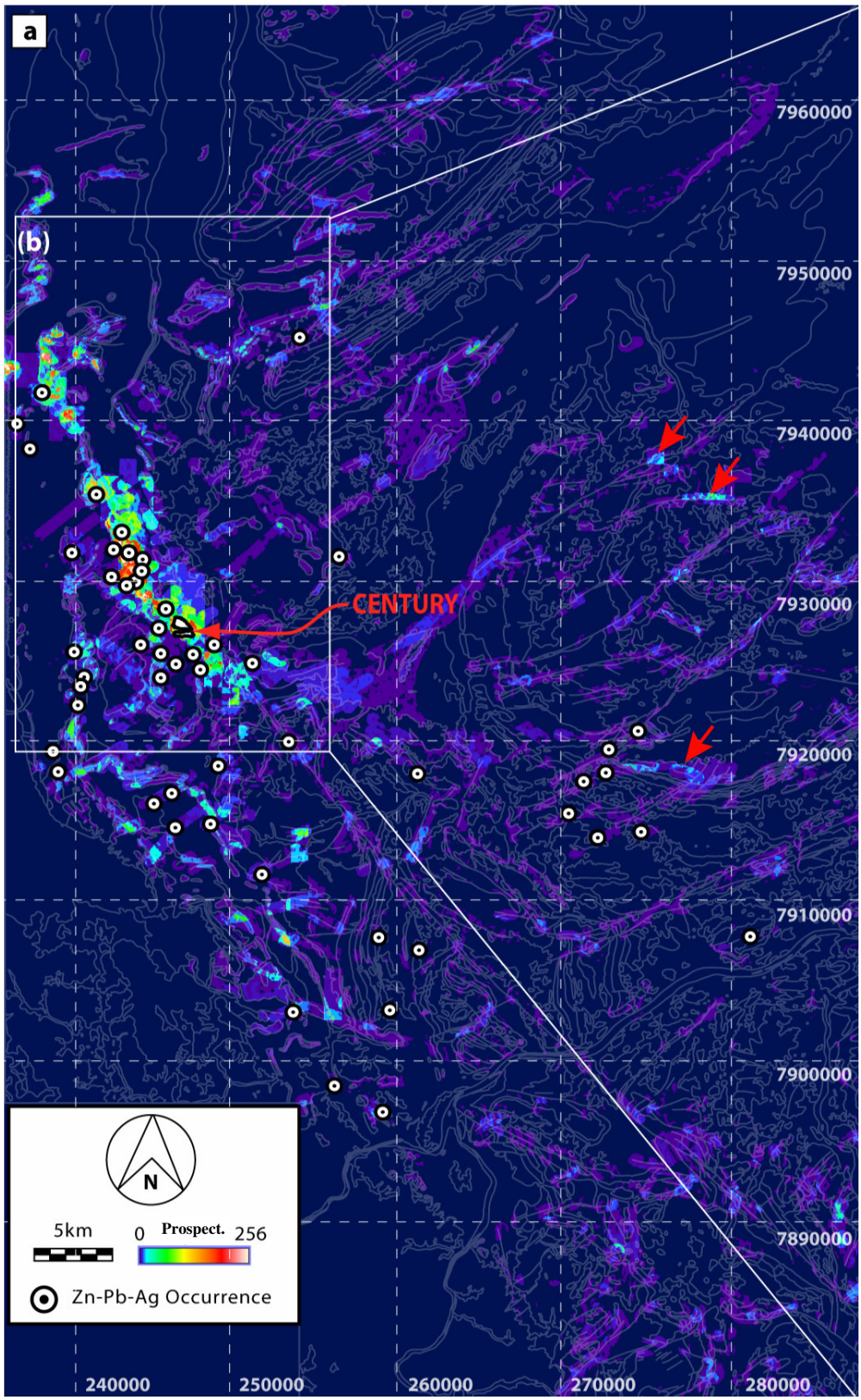
a
(b)
CENTURY
7960000
7950000
7940000
7930000
7920000
7910000
7900000
7890000
240000
250000
260000
270000
280000
N
5km
0
Prospect.
256
Zn-Pb-Ag Occurrence

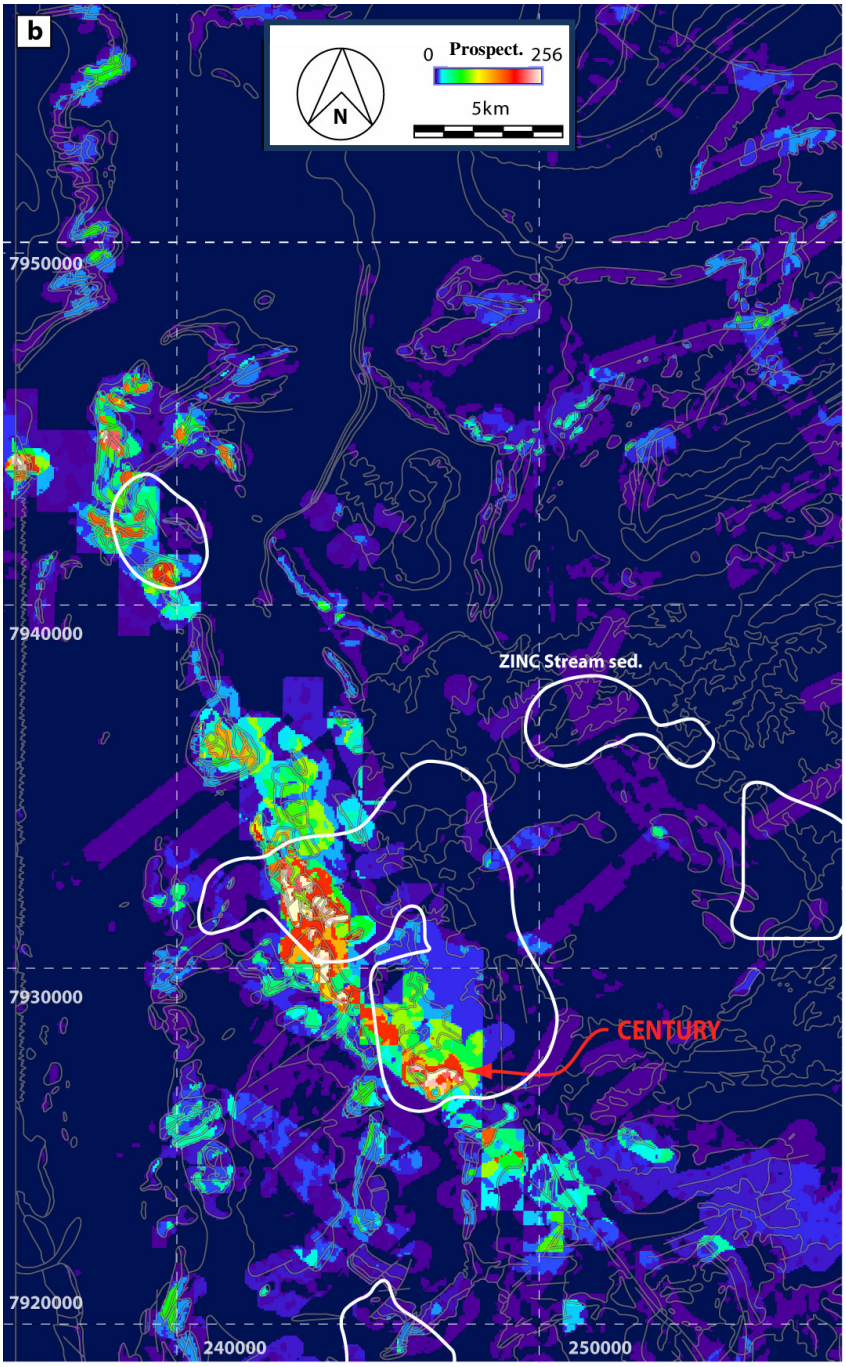

Fig. 3.20 Output of data driven modelling considering 11 layer (3 rejections) considering missing information related to cover sediments (QTJ – see Fig. 3.1a). (a) Data-driven model compared against known mineral deposits/prospects. Note the high potential along the Termite Range Fault, which was expected considering that clusters of known deposits are located in this area. However, local highs (although with lower values) are found in the Kamarga Dome area (see arrows). (b) Enlargement of Century area showing comparison of high-probability sites with geochemical stream sediment data (anomalies above 100 ppm of Zn content are indicated as closed polylines).

3.7. Conclusions

Constructed models were used to derive inferences relative to the two problems introduced in the first section of this chapter. These concern the definition of prospective areas for exploration and the possible "probabilistic" implications for the genesis of the different styles of mineralisation occurring in the Lawn Hill Region. The first point was addressed making use of pixel based algebra with a Boolean AND operation. Three final maps of favourability were constructed using this combination rule (Fig. 3.21a, b and c). Maps represent the integration of the KD- and DD-model for the SEDEX- and VS mineralisation. A third map was developed differentiating the integrated maps (KD + DD) for SEDEX and VS to obtain a final plot of the maximum likelihood of finding SEDEX-style or VS ore. The final model has constrained high favourability targets proximal to known occurrences. Other Century-style mineralisation might be located 7 km north of the "Edge" cluster (Fig. 3.21c). This apparently high P_{post} zone has similar values to Century, occurs in Pmh4, and is intersected by a NW fault which is parallel to and might be part of the Termite Range Fault termination.

This approach has limited application to ore genesis interpretations. It is however remarked that both KD-models and their integration show that the Century deposit is localised within a domain in which there is higher-favourability to locate SEDEX-style mineralisation, although VS ore could be present as well - meaning that the probabilistic approach is predicting both styles, but suggesting a higher proportion of SEDEX rather than VS ore.

Model results therefore partly reflect a previous study of this giant ore deposit (see Feltrin et al., 2006), which proposed that Century is more likely an exhalative to early-

diagenetic system with a component of later syntectonic mineralisation. It is also interesting to note that a comparison between the KD- and DD-probabilistic results provide an indication of scarce DD-mineral potential for areas where VS mineralisation would be favoured, based on KD-model results. This discrepancy might be due to undiscovered occurrences in VS-favourable domains or it could be interpreted as a lack of a major VS (syntectonic) fluid flow event in the region. In other words, if the later orogenic phase was only a minor "redistributing event", with only local circulation of fluids, then this would also explain the clustering of small VS occurrences observed around Century.

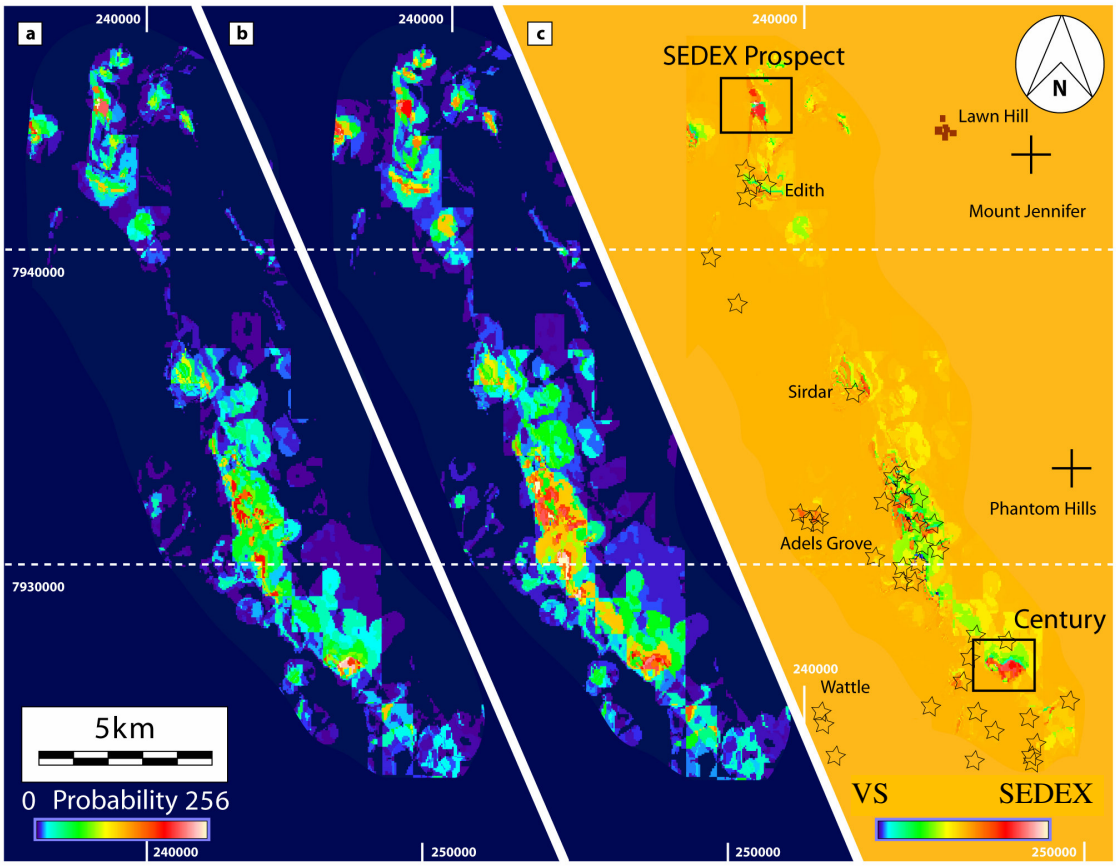

Fig. 3.21 Comparison of integrated KD-DD models. (a) SEDEX model. (b) VS model. Difference between the two total models is outlined in (c). The first two models offer similar results although local differences (km-scale) can be used to discriminate on a probabilistic ground between areas of elevated mineral potential for SEDEX or VS. A potential SEDEX target is outlined because of its similar favourability values to the Century deposit.